Selective synthesis and crystal chemistry of candidate rare earth Kitaev materials: honeycomb and hyperhoneycomb Na_2PrO_3

Ryutaro Okuma[*1,2], Kylie Macfarquharson[1], and Radu Coldea[1]

[1]Clarendon Laboratory, University of Oxford Physics Department, Parks Road, Oxford OX1 3PU, United Kingdom

[2]Institute for Solid State Physics, University of Tokyo, Kashiwa, Chiba 277-8581, Japan

*corresponding author: rokuma@issp.u-tokyo.ac.jp

Abstract: Rare earth oxides have gained interest as a platform to study frustrated magnetism arising from bond dependent anisotropic interactions. Ordered rock salt compounds Na_2PrO_3 crystallize in two polymorphs (α- and β) comprising honeycomb and hyperhoneycomb lattices of octahedrally coordinated Pr^{4+} ($4f^1$). Although possible realization of antiferromagnetic Kitaev interactions is anticipated for these phases based on *ab initio* models, air-sensitivity of the two polymorphs has hampered reliable crystal growth and physical property measurements. Here, we have succeeded in powder and single crystals of both α- and β-Na_2PrO_3 using modified synthetic procedures. Revised crystal structures for both polymorphs are obtained from refinement of un-twinned single-crystal X-ray diffraction data.

INTRODUCTION

Frustrated spin interactions between quantum spins are expected to stabilize under certain circumstances a macroscopically entangled ground state with fractional spin excitations, called a quantum spin liquid[1-3]. The Kitaev model on the honeycomb lattice is one of few exactly solvable models of a two-dimensional quantum spin liquid, in which each spin feels three types of Ising interactions depending on the bond direction[4]. After the proposal that the Kitaev model could be realized in transition metal oxides with large spin orbit coupling[5-7] numerous honeycomb magnets based on Ir^{4+} ($5d^5$) and Ru^{3+} ($4d^5$) have been explored[5-7] and evidence for substantial bond dependent interactions[8] and unconventional thermal transport[9] and continuum of magnetic excitations[10] have been observed. Key ingredients for the exotic interactions are spin-orbit entangled j_{eff}-1/2 degrees of freedom and edge-shared octahedra of the magnetic ions. Extension of the Kitaev model to three-dimensional lattices that maintain the local-three-fold coordination of each site keeps the model exactly solvable[11] and brings new physics[12], although realization of such lattices in real materials is very limited, to β-Li_2IrO_3[13, 14] and γ-Li_2IrO_3[15, 16], and site-disordered β-$ZnIrO_3$[17]

Lanthanide Kitaev magnets 4*d* and 5*d* transition metal oxides have been widely established as a platform for exhibiting anisotropic magnetism due to an inherent strong spin-orbit coupling. Similar bond-dependent interactions can be in principle also be realized in rare-earth 4*f* ions. This is because the ground state wavefunctions for $4f^1$ ions can also realize a $j_{\text{eff}} = 1/2$ Kramers ground state doublet in an octahedral cubic crystal field environment[18]. However, the large ionic radius makes it uncommon to have octahedral coordination by oxygen atoms as exemplified by 8-fold coordination in pyrochlore oxides[19]. Octahedral coordination of lanthanides is typically found for the smallest magnetic lanthanide Yb^{3+} or for larger anions such as chalcogenides (S^{2-}, Se^{2-}, and Te^{2-}) and halides (Cl^-, Br^-, and I^-). Two-dimensional triangular lattice compounds with delafossite structures[20-23] and honeycomb lattice halides[24-26] of lanthanides have recently gained attention in the context of frustrated quantum magnetism. Recent *ab-initio* calculations proposed that rare-earth ions connected by edge-shared octahedra[27-30] could potentially realize much elusive *anti*ferromagnetic Kitaev interactions, predicted theoretically to stabilize much richer phase diagrams in applied field than systems with ferromagnetic Kitaev interactions.

Tetravalent lanthanides Another way to make lanthanides with octahedral coordination is to use a tetravalent state, such as found in the case of binary oxides LnO_2 with *Ln* = Ce, Pr and Tb. Pr^{4+} ($4f^1$) is of particular interest because it has a Kramers ground state doublet with an effective $j_{\text{eff}} = 1/2$ and comparable ionic radius of 0.85 Å to that of Ir^{4+} (0.765 Å)[31]. Indeed, there are three known polymorphs of Na_2PrO_3, two of which have honeycomb[32-34] and hyperhoneycomb[35] lattices of edge-sharing $Pr^{4+}O_6$ octahedra as found in α-[36] and β-[13, 14] Li_2IrO_3. In the latter the magnetic ions form a hyperhoneycomb lattice, which has the same local three-fold coordination as the planar honeycomb, but where additional bond rotations make it a three-dimensionally connected lattice. The third polymorph[37] of Na_2PrO_3 has a cubic rock salt structure with completely random arrangement of the cations in ratio Na:Pr = 2:1 on the same crystallographic site. Hyperhoneycomb β-Na_2PrO_3 was originally synthesized only in very small single crystal form and proposed to have a monoclinic space group of *C*2/*c* with full order of Na and Pr[35]. The structure of honeycomb α-Na_2PrO_3 was proposed to be described by a (different) *C*2/*c* unit cell with substantial disorder between Na and Pr because powder samples suffer from layer stacking faults and no single crystals have yet been available[32, 34]. So far, physical properties have been investigated only in powder samples of α-Na_2PrO_3[32, 34]. The synthesis and experimental investigation are both challenging because of the moisture sensitivity of Na_2PrO_3 and of the starting chemicals.

We have recently succeeded[38] in production of β-Na_2PrO_3 by removal of low-melting impurities that favor α-Na_2PrO_3. In this present study, we extended this strategy to obtain single-crystalline α-Na_2PrO_3 and revise the crystal structure based on x-ray diffraction from a disorder-free, untwinned

single crystal. We describe the synthetic protocols to separately obtain all three polymorphs of Na_2PrO_3, provide a comprehensive study of the influence of synthesis parameters on the growth of single crystals of both α- and β-phases and compare the structural and magnetic similarities of both phases.

EXPERIMENTAL SECTION

Powder synthesis of α- and β-Na_2PrO_3. All samples were handled inside a nitrogen filled glovebox. Polycrystalline samples of α- and β-Na_2PrO_3 were synthesized either by annealing cubic Na_2PrO_3 or by a direct solid-state reaction between Na_2O_2 and Pr_6O_{11}. The cubic polymorph was first synthesized by a conventional solid-state reaction of Na_2O_2 (Alfa Aesar, 95%) and Pr_6O_{11} (Merck Life Science, 99.9%). Because as-received Pr_6O_{11} contains PrO_2 and unidentified phases, it was calcined in air at 800˚C for 24 hours to obtain phase-pure Pr_6O_{11}. In a typical synthesis, 1.3 mmol of Pr_6O_{11} and 8.6 mmol of Na_2O_2, which amounts to 10 mol% excess use of Na_2O_2, was thoroughly ground and pelletized. The pellet was loaded in an evacuated (P < 1 Pa) 40 cm long φ = 17 mm diameter fused silica tube. The ampoule was placed in a horizontal furnace and reacted at 400˚C for 48 hours. The heated sample contained purely the cubic phase, weighing 1.8 g. The heating time was determined such that no Na_2O_2 remained in the mixture after the reaction. The polycrystalline cubic phase sample was thoroughly ground, pelletized, and loaded in an open silver tube inside the glovebox. The silver tube was sealed inside an evacuated fused silica tube and reacted at 600˚C and 800˚C for 12 hours to obtain powder α- and β- phases, respectively. The direct solid-state reaction between Na_2O_2 and Pr_6O_{11} was performed for both Na-deficient and Na-excess mixtures; the thoroughly ground powder was pressed into a pellet, loaded in an open silver tube, sealed in an evacuated fused silica tube, and reacted at elevated temperatures. Samples obtained by annealing the cubic phase were used for the physical properties measurements.

Single crystal growth of α- and β-Na_2PrO_3. All samples were handled inside a nitrogen filled glovebox except Pr_6O_{11}. Single crystals of α- and β-Na_2PrO_3 were synthesized by a solid-state reaction of Li_2O (Alfa Aesar, 99.5%), Na_2O (Alfa Aesar, 80%), and PrO_2. PrO_2 was synthesized by heating calcined Pr_6O_{11} in O_2 flow at 280˚C for 4 weeks. Li_8PrO_6 was synthesized by heating stoichiometric mixture of as-received Pr_6O_{11} and Li_2O in O_2 flow at 700˚C for 24 hours. In a typical synthesis, 0.8 mmol of PrO_2, 1.6 mmol of Na_2O, and 3.2 mmol of Li_2O, were ground and pressed into a pellet of φ = 5 mm in diameter. The pellet was placed in a 5 cm long silver tube of φ = 6 mm in diameter. One side of the silver tube was sealed by flame before loading the pellet and the other side was mechanically sealed inside the glovebox after loading it and finally securely sealed by flame. The pellet was sealed in an evacuated quartz tube. The ampoule was placed in a box furnace and reacted at 750˚C for more than two weeks and less than a month. Rhombic dark brown crystals of β-Na_2PrO_3 with a developed ab plane of the largest area of 0.5 mm^2 grew on the surface of the pellet and smaller crystals were found inside. The crystals were surrounded by yellow crystals of Li_8PrO_6 and colorless crystals of Na_2O. The rhombic crystals were mechanically extracted from the pellet. A small amount of α-Na_2PrO_3 formed as very thin crystals with a diameter up to 200 μm. Addition of NaOH made by hydration of Na_2O yielded only α-Na_2PrO_3 crystals.

Characterization. Powder X-ray diffraction (XRD) analysis was performed to confirm the purity of the samples using a Panalytical X'pert diffractometer (monochromatic Cu $K\alpha_1$, λ = 1.54056 Å). To prevent contact with air the specimen was prepared in a nitrogen filled glovebox and placed in a dome shaped sample holder sealed inside the glovebox. The data were collected within the 10−60° 2θ range with a step of 0.02°. The FullProf Suite was used for structural refinement[39]. Single crystal XRD measurements were performed on an Oxford Diffraction Supernova diffractometer at room temperature operating at Mo $K\alpha$, λ = 0.71073 Å. Crystals of the β-phase were covered with Dow Corning vacuum grease and no obvious decomposition was observed during the maximum measurement time of two hours. Crystals of the α -phase were sealed under vacuum inside a glass capillary, after first coating them in a thin layer of melted paraffin such that they could be stuck in a fixed position on the glass capillary. The X-ray data were collected and reduced using the CrysAlisPro software. Absorption corrections were made empirically. Initial models of the crystal structures were obtained with the program SIR-2014[40] and refined using the program Olex2[41]. Extinction corrections were applied by scaling the observed structure factor $|F_{obs}|$ to $|F_{calc}|/[1+\xi*0.001|F_{calc}|^2\lambda^3/\sin(2\theta)]^{1/4}$, where ξ was refined. The atomic displacement parameters were refined anisotropically. VESTA was used for the structure visualization[42].

Magnetometry. Magnetization measurements were performed using a Quantum Design MPMS3 system in fields up to 7 T and temperatures down to 2 K, first on powders and subsequently on co-aligned single crystals of the β-phase with a total combined mass of ~1 mg on a diamagnetic substrate. The single crystal susceptibilities showed contribution from the ferromagnetic impurity phase Pr_6O_{11} due to decomposition on the surface, which was subtracted by comparing the magnetization data to single-crystal torque magnetometry data reported elsewhere[38].

RESULTS AND DISCUSSION

Crystal growth. Tables I and II summarize various synthetic conditions to obtain powder and single crystals of α- and β-Na_2PrO_3. We first describe the powder synthesis in detail and then discuss the single crystal growth. In previous studies of Na_2PrO_3, the powder sample of α-Na_2PrO_3 was prepared by the reaction of Pr_6O_{11} with Na_2O_2 or Na_2O under O_2 flow condition[32-34] at 600˚C-700˚C. Two reaction routes[35] under sealed condition were employed for β-Na_2PrO_3, namely an ion exchange reaction between Na_2O and Li_8PrO_6 at 700˚C or a direct solid-state reaction of Pr_6O_{11} with slightly excess Na_2O_2 at 650˚C. The critical difference between the O_2 flow reaction and the sealed condition is contamination of Na_2O or Na_2O_2 by water. Continuous flow of oxygen is expected to introduce substantial amounts of moisture over time and to produce NaOH. To prevent the degradation of sodium oxides, we used sealed conditions except for the purpose of reproducing the previous studies. The basic trend found in this study was that melt stabilizes α-Na_2PrO_3 although β-Na_2PrO_3 seems to be the more stable phase, which can be understood from Ostwald ripening of crystal growth. NaOH and Na_2O_2 melt at 318˚C and 675˚C, respectively, meaning that they need to be consumed below the temperature at which β-phase starts to form (~550˚C). Although the direct reaction of Na_2O_2 and Pr_6O_{11} seems most simple, it results in a mixture of α- and β-Na_2PrO_3 because of the above-mentioned reason. The most reproducible and scalable procedure to produce the β-phase is to make pure cubic phase with low crystallinity at low temperature and anneal it at 800˚C; a lower temperature of 600˚C resulted in the α-phase. The powder diffraction pattern of each phase is presented in Figure 1.

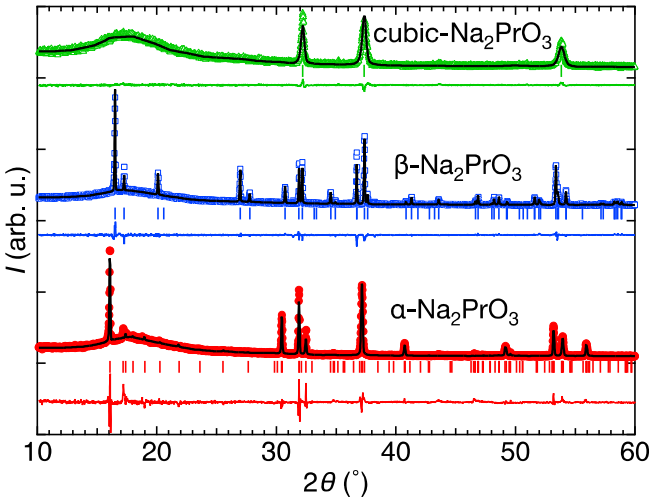

Figure 1. XRD powder diffraction patterns of the three polymorphs of Na_2PrO_3, offset vertically for clarity (data reproduced from Ref.[38]). Red circles, blue squares, and green triangles represent the powder diffraction pattern of α-, β-, and cubic-Na_2PrO_3. Black lines and bars under each data set indicate fits to Rietveld refinement and positions of Bragg peaks of each phase. Red, blue, and green lines are the residual of the fits of each phase. Details of the refinements are presented in Table III with structural parameters listed in Tables IV and V.

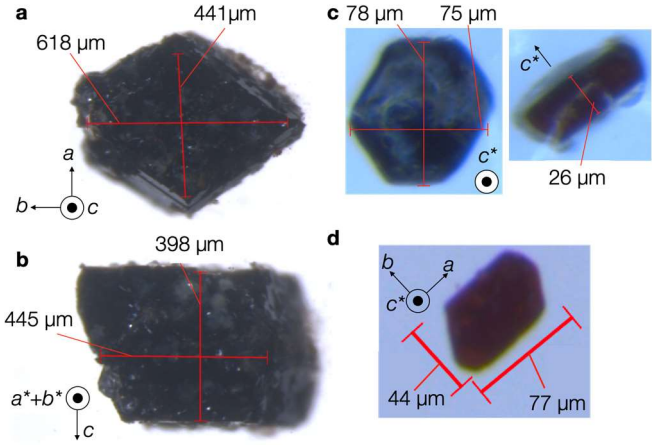

Figure 2. Optical microscope images of single crystals of α- and β-Na_2PrO_3. **a**, The largest grown β-Na_2PrO_3 crystal viewed along (001). **b**, The same β-Na_2PrO_3 crystal viewed along (110). **c**, Hexagonal shaped twinned crystal of α-Na_2PrO_3 viewed along c^* (left image) and a perpendicular direction (right image). The color appears denser when viewed perpendicular to the honeycomb plane. **d**, Single grain, untwinned α-Na_2PrO_3 crystal with an elongated shape along the monoclinic a axis.

For single crystal growth of the α- and β-Na_2PrO_3, all the attempts to crystallize them by a flux method failed; mixture of Pr_6O_{11} and excess NaF and Na_2O_2 formed crystals of the cubic phase. As noted in the previous study[35], the intermediate compound Li_8PrO_6 is key to stabilization of the β-phase. More specifically, Li_2O works as a mineralizer for formation of the β-phase because it was found that addition of Li_2O converts the α-phase to the β-phase. The largest single crystal of β-Na_2PrO_3 was prepared by reaction of Li_2O, Na_2O, and PrO_2 instead of using Li_8PrO_6. The advantage of PrO_2 over Li_8PrO_6 is insensitivity to moisture. Although Li_8PrO_6 slowly decomposes in moist air, it is typically prepared under oxygen flow condition and inevitably contains a small amount of LiOH. Such a low melting hydroxide is unfavorable for formation of the β-phase. Single crystals of α-Na_2PrO_3 were found as a minority phase in the β-phase or predominantly formed by addition of NaOH. Figure 2 presents pictures of single crystals of each phase. Large crystals of β-phase have a rhombic shape with each edge corresponding to one of the **a±b** unit cell diagonals (Figs. 2a-b). The α-phase crystals always form as thin platelets, hexagonal ones as shown in Fig. 2c (left image) tend to contain multiple structural twins rotated by 120° around a common c^* axis. Single grain, untwinned α-crystals are elongated along the monoclinic a axis with a typical crystal shape morphology shown in Fig. 2d. Small crystals of both phases look similar but only the α–phase crystals display significant pleochroism, they appear transparent brown when viewed along an in-plane direction ($\perp c^*$) but very dark in the out-of-plane direction ($//c^*$).

Table I. Selected synthetic condition to obtain polycrystalline powder of the three polymorphs of Na_2PrO_3, bold highlighting corresponds to the conditions used to produce the highest-purity β-Na_2PrO_3 powder used for the x-ray diffraction in Fig. 1 (lower trace) and magnetic susceptibility in Fig. 8. Evacuated quartz tubes are used for reaction vessels in addition to open silver tubes inside the quartz tubes for the reaction temperature higher than 500˚C.

Starting materials	Reaction condition	Phase analysis
$x$$Na_2O_2$ (x > 1), 1Pr_6O_{11}	350-450˚C, 24-96 hours	Cubic-Na_2PrO_3, Na_2O_2
$x$$Na_2O_2$ (x > 1), 1Pr_6O_{11}	550-640˚C, 12 hours	α- and β-Na_2PrO_3, NaOH, PrO_2
$x$$Na_2O_2$ (x < 1), 1Pr_6O_{11}	800˚C, 12 hours	β-Na_2PrO_3, NaOH, PrO_2
$x$$Na_2O_2$ (x > 0.1), 1cubic-Na_2PrO_3	550˚C-800˚C, 12 hours	α-Na_2PrO_3
$x$$Na_2O$ (x > 0.1), 1cubic-Na_2PrO_3	550˚C-800˚C, 12 hours	α-Na_2PrO_3
$x$$Na_2O_2$ (x < 0.1), 1cubic-Na_2PrO_3	**800˚C, 12 hours**	**β-Na_2PrO_3, NaOH**
0.1Li_2O, α-Na_2PrO_3	800˚C, 12 hours	β-Na_2PrO_3, Li_2O

Table II. Selected synthetic condition to obtain single crystals of the three polymorphs of Na_2PrO_3, bold highlighting corresponds to the conditions used to obtain the largest size β-Na_2PrO_3 crystal shown in Fig. 2ab.

Starting materials	Reaction condition	Single crystals
$x$$Na_2O$ (x < 2), 1Li_8PrO_6	650-750˚C, 2-8 weeks, sealed Ag	α- and β-Na_2PrO_3
$x$$Na_2O$ (x > 2), 1Li_8PrO_6	650-750˚C, 2-8 weeks, sealed Ag	Unknown phase (Na_xPr_yO with x/y>2)
1Na_2O_2, 1Li_8PrO_6	650˚C, 2-8 weeks, sealed Ag	α- and β-Na_2PrO_3
1Na_2O_2, 1Li_8PrO_6	700˚C, 2-8 weeks, sealed Ag	α-Na_2PrO_3
2Na_2O_2, 2NaF,1PrO_2	Cooling from 700˚C by -5˚C/hr, sealed Ag	cubic-Na_2PrO_3
$x$$Na_2O$ (x < 2), 4Li_2O, 1PrO_2	**650-750˚C, 2-8 weeks, sealed Ag**	**α- and β-Na_2PrO_3**
1.1Na_2O_2, 1Li_8PrO_6	650-750˚C, 2-8 weeks, O_2 flow on Au foil	α- and β-Na_2PrO_3, Li_2PrO_3

Table III. Rietveld refinement results for the powder X-ray data on the three phases of Na_2PrO_3 plotted in Fig. 1. The atomic positions and isotropic U_{iso} values are fixed to those values obtained from the single crystal refinement results given in Tables IV and VI. Calculations of the pattern of the α-phase was performed for the partially disordered structure in which the Na1 and Pr1/Pr2 sites are partially occupied by Pr and Na, respectively, as per Table V, with the positions of the other atoms fixed to those in Table IV. The refined partial occupancy of Na1 and Pr1/Pr2 sites is 54.7(6)% and 77.4 (3)% respectively[32]. In the cubic phase, Na/Pr and O are placed in the 4*a* (0 0 0) and 4*b* (1/2 1/2 1/2) positions, respectively, in which the occupancy of 4*a* site by Na and Pr is fixed to 67% and 33%, respectively. For β-Na_2PrO_3 we used the structural model in Table VI. Use of the dome-shaped sample holder caused a substantial increase in the background signal, leading to higher R_{exp} after background correction. R_{exp} without background correction is 8.14%, 5.78, and 8.49 for β, α, and cubic phases, respectively.

Phases	R_p, R_{wp}, R_{exp} (%)	Space group and unit cell parameters
α-Na_2PrO_3	34.9, 27.3, 15.4	$C2/c$, a = 5.9586(2) Å, b = 10.3297(3), c = 11.2063(3) Å, β = 100.328(1)˚
β-Na_2PrO_3	27.5, 24.3, 16.6	$Fddd$, a = 6.7613(3) Å, b = 9.7812(4) Å, c = 20.5313(9) Å
cubic-Na_2PrO_3	22.5, 22.3, 15.0	$Fm\bar{3}m$, a = 4.8166(6) Å

Crystal structure determination. The crystal structure of α-Na_2PrO_3 was determined using single crystal X-ray diffraction data at room temperature. Results of the structural refinement are summarized in Table IV. We first describe the revised α-phase crystal structure and then compare the local coordination in both α- and β-structures.

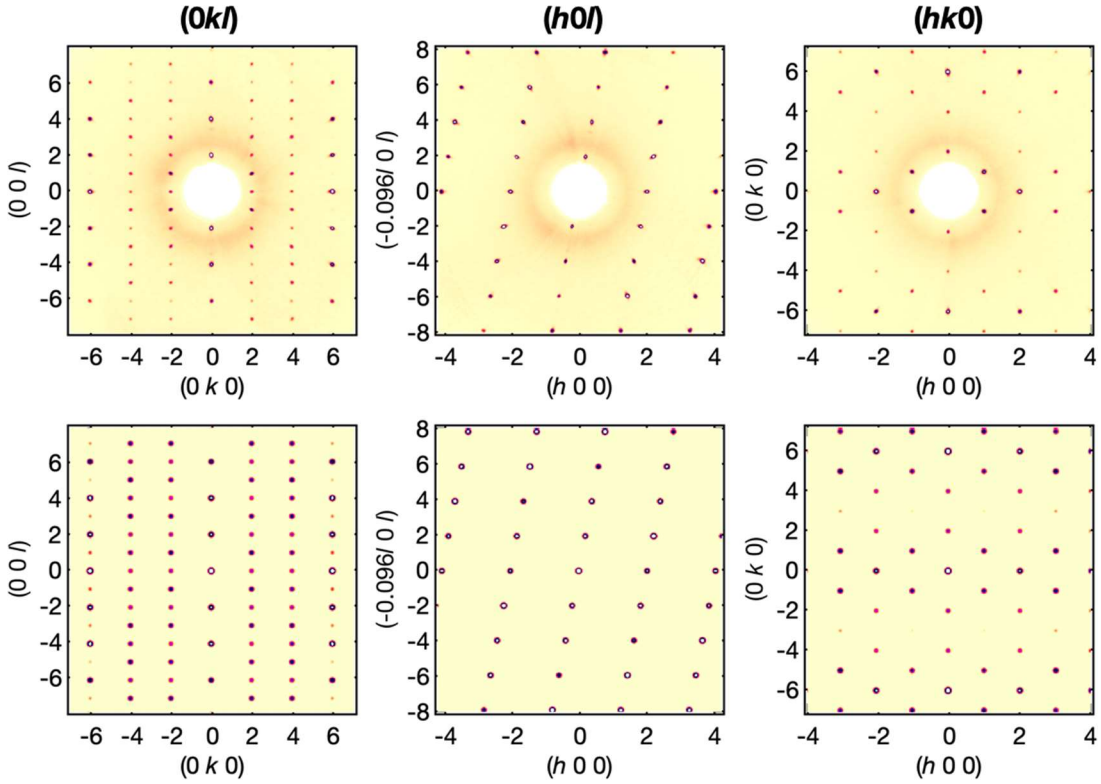

Figure 3. X-ray diffraction patterns of an untwinned α-Na_2PrO_3 single crystal. (top) Observed patterns in the 0*kl*, *h*0*l*, and *hk*0 planes in the region with scattering wavevector $|Q| < 4.5$ Å^{-1}. (bottom) Calculated X-ray diffraction patterns based on the refined structural model in Table IV. *C*-centering requires the sum $h + k$ to be even and the *c*-glide (mirror in the (x0z) plane followed by translation by **c**/2) forbids odd l reflections in the *h*0*l* plane. The halo around the origin is due to scattering from the vacuum sealed glass capillary inside which the crystal was placed. All observed diffraction peaks are sharp with no detectable diffuse scattering rods along l, indicating the absence of layer stacking faults, common in powder samples of α-Na_2PrO_3[32,34] as well as other layered honeycomb systems such as Na_2IrO_3[43].

For the α-phase, elongated crystals as in Fig. 2d showed no apparent twinning or stacking faults. The previous powder study[32,34] proposed a monoclinic space group of *C*2/*c* with unit cell lattice parameters $a_p \sim 5.96$ Å, $b_p \sim 10.3$ Å, $c_p \sim 11.7$ Å, and $\beta_p \sim 110^\circ$. In our study, we use a revised monoclinic unit cell with angle $\beta \sim 100^\circ$ much closer to 90°. The revised unit cell basis vectors ***a, b, c*** are related to the previously proposed[32,34] unit cell basis vectors $\boldsymbol{a}_p$, $\boldsymbol{b}_p$, $\boldsymbol{c}_p$ as follows: $\boldsymbol{a} = \boldsymbol{a}_p$, $\boldsymbol{b} = -\boldsymbol{b}_p$, and $\boldsymbol{c} = -\boldsymbol{a}_p - \boldsymbol{c}_p$. This transformation does not involve a space group change. To illustrate the validity of the revised unit cell, single crystal x-ray diffraction patterns in the 0*kl*, *h*0*l*, and *hk*0 planes are presented in Fig. 3 (top row). Throughout we index reflections in terms of Miller indices with reference to the crystallographic (revised) unit cell. The diffraction patterns have 2-fold rotation symmetry around (010) (normal to panels in Fig. 3 middle column) and mirror symmetry normal to this axis (inspect diffraction patterns in the left and right columns), leading to a 2/*m* Laue class. All observed peaks satisfy the selection rule $h+k$ even as expected for a *C*-centered cell The above two considerations narrow down the possible space groups to *C*2/*c* or *C*2/*m*. Those could be differentiated by the pattern in the *h*0*l* plane (Fig 3. middle column), which clearly observe systematic absences at l = odd, as expected for a *C*2/*c* space group and attributed to the *c*-glide. The correct choice for the *c* lattice parameter is demonstrated by the presence of odd l reflections in the 0*kl* diffraction pattern (left column).

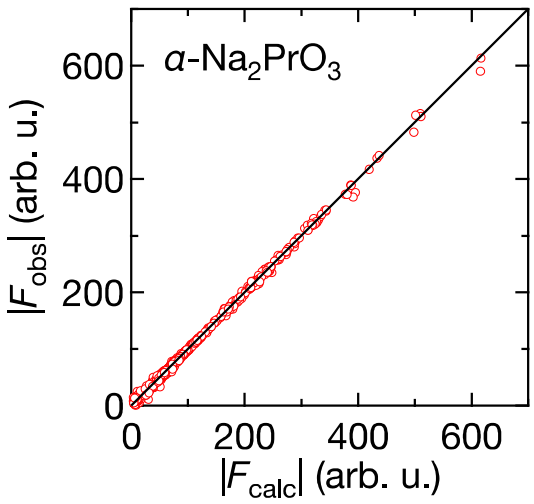

Figure 4. Observed vs calculated X-ray structure factor for the refined structural model for α-Na_2PrO_3 in Table IV. Solid line shows the 1:1 agreement.

Crystal structure refinement of the α-phase converged to the expected Pr honeycomb structure in the monoclinic *ab* plane (see Fig. 5a) and the obtained atomic coordinates are listed in Table IV. This revised crystal structure of α-Na_2PrO_3 is isostructural to Na_2TbO_3[35]. The calculated diffraction patterns agree well with the observed ones as Fig. 3 shows, compare top and bottom rows. Observed and calculated X-ray structure factors are quantitatively compared in Fig. 4. The refined crystal structures of both α- and β-Na_2PrO_3 are schematically illustrated in Figure 5. Both polymorphs have ordered rock salt structures with no disorder in the

arrangement of sodium and praseodymium. Based on our single crystal results in α-Na_2PrO_3, two-dimensional honeycombs form by edge-sharing of two structurally non-equivalent PrO_6 (dark/light) blue octahedra illustrated in Fig. 5a. Compared with the honeycomb iridate α-Li_2IrO_3 with a single honeycomb layer per unit cell and single Ir site, the crystal structure of α-Na_2PrO_3 has a two layer stacking periodicity, with the two layers in the unit cell related by a *c*-glide (mirror in the *ac* plane followed by translation by ***c***/2), so the inter-layer spacing is roughly doubled compared to α-Li_2IrO_3. One of the sodium sites Na1 sits at the center of the honeycombs and the Na2 and Na3 sites form a hexagonal lattice in-between stacked honeycomb layers as plotted in Fig. 5b. The displacement parameters of sodium atoms are much more anisotropic than those of the other atoms; the thermal ellipsoid of Na1 is elongated towards *c** and those of Na2 and Na3 are more elongated in-plane presumably because Na is less likely to move towards the heavy Pr atoms.

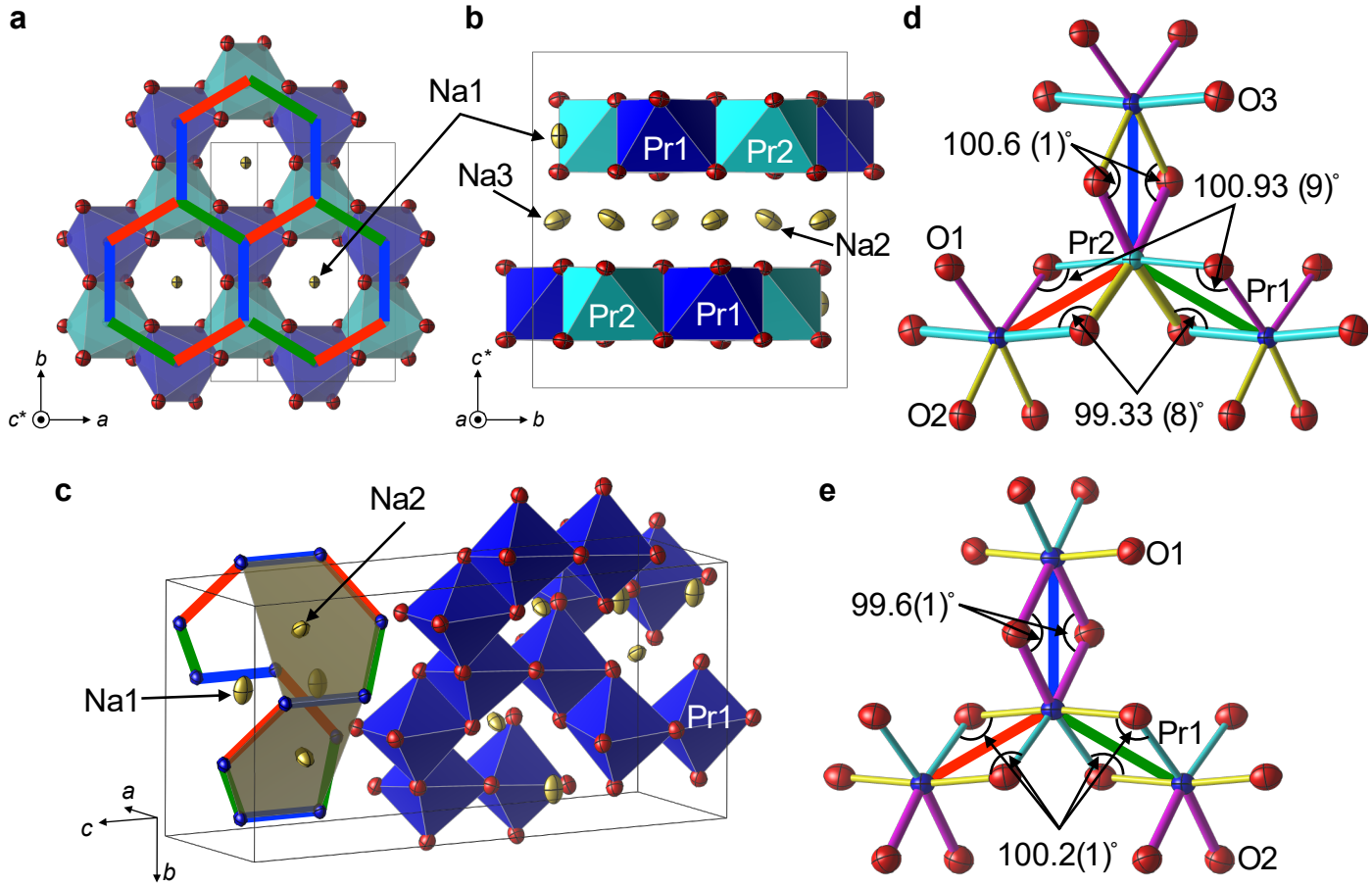

Figure 5. Crystal structures of α- and β-Na_2PrO_3. Light/dark blue, yellow and red ellipsoids represent praseodymium, sodium, and oxygen atoms, respectively, scaled by their anisotropic displacement parameters U_{ij}. The probability that nuclei are included in the interior of the ellipsoid is 99%. (a) Connectivity of PrO_6 in the α-phase in the *ab* plane. Alternating Pr1/Pr2 sites form a honeycomb network. The unit cell outline is shown by thin black lines. (b) Stacking of the honeycomb planes in α-phase. (c) Connectivity of PrO_6 octahedra in the β-phase (using atomic positions from Ref.[38]). Red/green/blue bond coloring in both a and c corresponds to the bond Ising **x**,**y**,**z** character in a Kitaev model for an ideal structural model where all octahedra are cubic and the three Pr-O2-Pr superexchange planes meeting at a site are mutually orthogonal, with **x**,**y**,**z** axes normal to those planes. (d) Edge-sharing connectivity of PrO_6 octahedra in d) α- and e) β-phases with bond angles indicated. Inequivalent Pr-O bonds are shown in different thickness and color. In both d) and e) two of the Pr-Pr bonds that share a site are symmetry-related (red and green) by a 2-fold axis along the third Pr-Pr bond (blue) that shares the same site.

For completeness we note than an ideal version of the crystal structure of α-Na_2PrO_3 with all octahedra cubic is obtained by a slight rescaling of the lattice parameters to be in the ratio $a : b : c = \sqrt{6} : 3\sqrt{2} : \sqrt{22}$, angle $\beta = \cos^{-1}(-1/\sqrt{33}) = 100.0\ldots^\circ$ and ideal atomic fractional coordinates Na1(0, 11/12 ,1/4), Na2(1/4, 1/4, 0), Na3(1/4, 7/12, 0), Pr1(0, 7/12, 1/4), Pr2(0, 1/4, 1/4), O1(1/8, 3/4, 1/8), O2(1/8, 5/12, 1/8), O3(1/8, 1/12, 1/8) with the set of axes $\mathbf{x} = -3\sqrt{2}\mathbf{a}/8b + \sqrt{2}\mathbf{b}/2b + 3\sqrt{2}\mathbf{c}/8b$, $\mathbf{y} = -3\sqrt{2}\mathbf{a}/8b - \sqrt{2}\mathbf{b}/2b + 3\sqrt{2}\mathbf{c}/8b$ and $\mathbf{z} = 9\sqrt{2}\mathbf{a}/8b + 3\sqrt{2}\mathbf{c}/8b$, normal to the three Pr-O-Pr superexchange planes meeting at every site.

In previous reports, Rietveld refinement of the α phase structure on powder sample proposed that 1/3 of one of the two Pr sites in the honeycomb plane was occupied by Na and the other Pr site was fully occupied by Pr[32], while local ordering of Na and Pr was suggested by pair distribution function (PDF) analysis[34]. This local structure suggested by the PDF analysis[34] extended to the case of no atomic site mixing (i.e. both nominally Pr sites fully occupied by Pr) is different from the structure in Table IV in that the positions of Na1 and Pr1 are swapped, however such a structure with those two sites swapped is not compatible with our single crystal x-ray data; attempts to refine our data in this structure increased $R_{wp,all}$ from 3.87% to 4.33% and resulted in unphysical, non-positive definite anisotropic displacement parameters.

Regarding the powder diffraction patterns, our data shows the same disorder effects as previous studies. Many diffraction peaks expected from the fully ordered *C*2/*c*

structure found in single crystals were not observed in the powder XRD data as shown in Fig. 6 (dashed line is the expected pattern using the fully-ordered crystal structure in Table IV). Indication of the *C*2/*c* structure appears only around the (1 1 0) position with *d*~5.1 Å, which is forbidden in a single-layer *C*2/*m* model, isostructural to α-Li_2IrO_3. Unit cell basis vectors of this single layer *C*2/*m* structure; $\boldsymbol{a}_s$, $\boldsymbol{b}_s$, $\boldsymbol{c}_s$, are related to those of the two-layer *C*2/*c* structure by the following relations $\boldsymbol{a}_s = \boldsymbol{a}$, $\boldsymbol{b}_s = -\boldsymbol{b}$, and $\boldsymbol{c}_s = -\boldsymbol{a}/2 - \boldsymbol{c}/2$. The powder pattern presented in Figs. 1 and 6 was fitted by allowing some finite occupation of Na on both of the two Pr sites and a finite occupation of Pr on the Na1 site in the honeycomb layer of the crystal structure of α-Na_2PrO_3 to mimic the effect of layer stacking faults. The site-mixing model above leads to the suppression /disappearance of many diffraction peaks and a significant reduction of the occupancy of the honeycomb center Na1 site by almost half, as summarized in Table V.

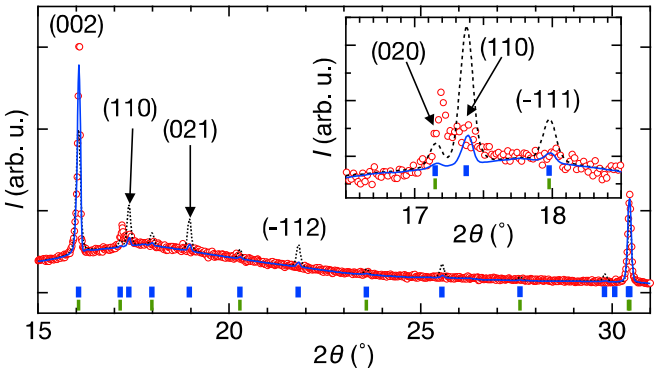

Figure 6. Diffraction pattern of polycrystalline α-Na_2PrO_3 phase shown by red points, compared with patterns calculated for the fully ordered structure in Table IV (black dotted line) and a partially ordered structure (blue line, same as in Fig. 1) as described in the text. Positions of Bragg peaks of the two-layer *C*2/*c* and single-layer *C*2/*m* structures described in the text are shown below the pattern in thick blue and thin green bars, respectively. Inset shows a closeup of the region near the position of the (110) diffraction peak disallowed in the *C*2/*m* structure. The peak indexing is with reference to the two-layer *C*2/*c* unit cell.

Regarding the crystal structure of the β-phase, a monoclinic unit cell with space group *C*2/*c* and lattice parameters a_m ~ 6.79 Å, b_m ~ 9.77 Å, c_m ~ 10.8 Å, and β ~ 108˚ was originally proposed in the original synthesis study[35]. We recently revised the crystal structure model based on analysis of an extensive single crystal x-ray diffraction data set. We find an orthorhombic unit cell of space group *Fddd* (a supergroup of *C*2/*c*) with lattice parameters a ~ 6.79 Å, b ~ 9.77 Å, and c ~ 20.6 Å. This revised crystal structure is isostructural to β-Li_2IrO_3, with refinement results presented in Table VI. β-Na_2PrO_3 features a full three-dimensionally linked network of PrO_6 octahedra connected via edge-sharing to form a hyperhoneycomb lattice. There is only one crystallographic Pr site and the hyperhoneycomb lattice comprises two families of zigzag chains running alternatingly along the basal plane diagonals $\boldsymbol{a} + \boldsymbol{b}$ and $\boldsymbol{a} - \boldsymbol{b}$ directions, connected by bonds along the c axis. Theoretical models that discuss the possible realization of a Kitaev spin model on the hyperhoneycomb lattice are based on an ideal crystal structure with all PrO_6 octahedra regular (cubic) and all Pr-O-Pr angles 90°, which can be obtained from the actual crystal structure in Table VI by scaling slightly the lattice parameters to have ratios a:b:c =1:√2:3 and displacing the ions slightly from their actual to ideal positions (for details see Ref.[38]). For this ideal structure the three Pr-O_2-Pr superexchange planes that meet at a Pr site are mutually orthogonal with normals along a Cartesian set of **xyz** axes expressed as $\mathbf{x} = (-\boldsymbol{a}/a - \boldsymbol{c}/c)/\sqrt{2}$, $\mathbf{y} = (\boldsymbol{a}/a - \boldsymbol{c}/c)/\sqrt{2}$ and $\mathbf{z} = -\boldsymbol{b}/b$, in relation to the idealized unit cell basis vectors. In the Kitaev model, each bond carries an Ising interaction between the magnetic moment components normal to the Pr-O_2-Pr plane of the bond. One can then color code all the bonds red/green/blue according to the **xyz** Ising character and we illustrate this by the color coding of the Pr-Pr bonds in Fig. 5c and e. Two crystallographically inequivalent sodium sites Na1 and Na2 fill the hollow of the plaquette. Na2 is located inside the incomplete honeycomb sections (shaded polygons in Fig 5c) formed by adjacent **z** - bonds connected via zigzag bonds and its displacement features out-of-plane motion as in the α-phase, while Na1, away from the incomplete honeycombs, has an ellipsoid elongated mainly along the b axis.

Despite the very different three-dimensional networks formed by the Pr ions in the two polymorphs, the local structural environments around the Pr ions closely resemble each other. Table VII presents the Pr-O bond lengths and Pr-O-Pr bond angles for α- and β-Na_2PrO_3. Figs. 5d and e illustrate the local threefold-coordinated geometry in the two phases. The Pr-Pr distances show relatively small variation in the range 3.422-3.444 Å, which is close to the corresponding value in the disordered cubic structure $a_c/\sqrt{2}$ ~ 3.406 Å. The Pr-O-Pr bond angles also take similar values for all the bonds, in the range 99-101°. The normals to the Pr-O_2-Pr planes that share a site make relative angles of 92.5˚ between **x-y** bonds and 91.8˚ between **y-z** and **z-x** bonds in the β phase and 91.5-92.1˚ for **x-y** bonds and 91.7˚-92.0˚ between **y-z** and **z-x** bonds in the α phase. The slight deviations of all those angles away from the ideal values of 90° indicate slight departures of the actual crystal structures from the ideal structures with cubic octahedra, where the three bonds sharing a site are connected by a local (pseudo) three-fold axis normal to the plane of the three bonds.

As the deviation of the bond angles from the ideal value of 90° is expected to lead to smaller Kitaev interactions, Fig. 7 compares the degree of distortion in candidate Kitaev honeycomb and hyperhoneycomb magnets. The deviation of bond angles in Na_2PrO_3 is comparable to Na_2IrO_3 and significantly larger than in α- and β-Li_2IrO_3 or α-$RuCl_3$. The distortion roughly correlates with the difference in ionic radii of the two cations in the rock salt structure; the ionic radii of the constituting elements are 0.76 Å, 0.765 Å, 0.85 Å, and 1.02 Å, for Li^+, Ir^{4+}, Pr^{4+}, Na^+, respectively, in octahedral (six-fold) coordination.

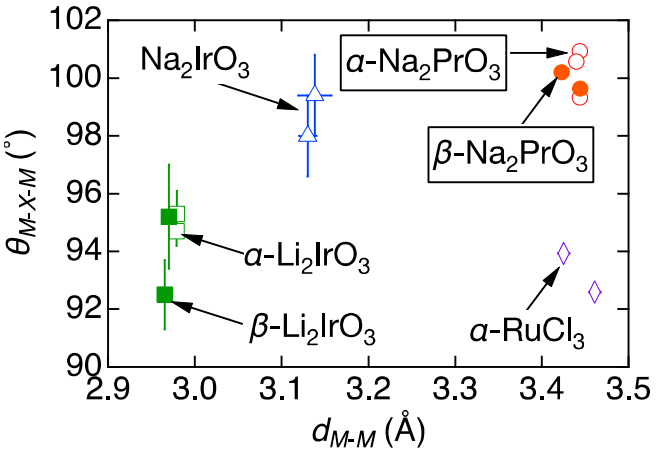

Figure 7. Comparison of bond lengths and angles of candidate Kitaev honeycomb and hyperhoneycomb materials. The distance between the nearest neighbor magnetic ions $d_{M\text{-}M}$ and the bond angle $\theta_{M\text{-}X\text{-}M}$ between two metal ions M and the coordinated anion X are plotted for M = Pr^{4+}, Ir^{4+}, Ru^{3+}, and X = O^{2-}, Cl^{-}. Green square, blue triangle, and purple diamond represent Na_2PrO_3, α- and β-Li_2IrO_3[14, 44], Na_2IrO_3[43], and α-$RuCl_3$[45] and open and filled red circles correspond to α- and β- Na_2PrO_3, respectively. Only the values of α-$RuCl_3$ are measured at 80 K, all others are taken from room temperature data.

Magnetic properties of α- and β-Na_2PrO_3

Powder and single crystal magnetization measurements were performed to investigate the magnetic properties of the β-phase. Susceptibility follows a Curie-Weiss law above 20 K. The effective moment and Weiss temperatures are 0.80(1)μ_B and -15(1) K, respectively. For the α-phase, a Curie-Weiss fit above 50 K yielded the effective moment and Weiss temperature of 1.08(1) K and –16(1) K, respectively, which are similar to the values obtained in the previous study[32]. The observed effective moments are reduced from, 10/7= 1.42… expected for the pure Γ_7 ground state doublet in the limit of very weak octahedral cubic crystal field relative to the spin orbit coupling[46]. Furthermore the spin interaction is large as insulating rare-earth compounds typically have exchanges of the order of 1 K[19]. These suggest the presence of a large hybridization between praseodymium and oxygen atoms because of the unusually high Pr valence. Recent studies found comparable energy scale of the crystal field and spin-orbit coupling in Pr^{4+} oxides[47, 48], which leads to mixing of the nominally j_{eff} = 1/2, Γ_7 doublet derived from the free-ion J = 5/2 multiplet with higher energy states derived from the J = 7/2 multiplet even in the cubic limit, with further mixing of more states when the local environment is distorted away from cubic, which is the case in both α- and β-Na_2PrO_3.

Temperature-dependent magnetic susceptibility measurements of β-phase powder and single crystals exhibit the same magnetic ordering temperature of 5.2 K as shown in Fig.8b. This excludes the possibility of Li contamination into Na sites and evidences good stoichiometry of our samples. Single crystal magnetization showed clear anisotropy below T_N of 5.2 K, suggesting that spins are predominantly aligned along the a axis. For the α-phase, we confirmed that it exhibits a weak ferromagnetic component that sets in spontaneously at T_N of 4.6 K, which is apparent in the upturn in the susceptibility both in powder and single crystals, as previously reported for powder samples[32,33]. More detailed investigations of the magnetic properties of the two phases will be reported in Ref.[38] and elsewhere.

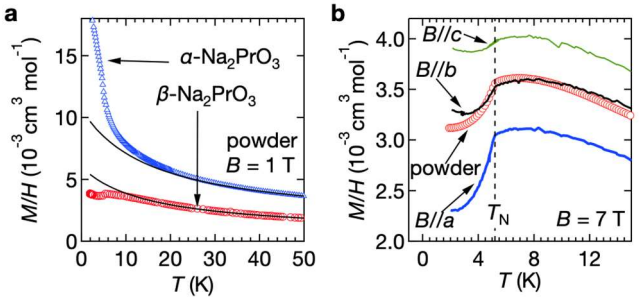

Figure 8 (a) Temperature dependence of magnetic susceptibility of α- and β-Na_2PrO_3 measured by field cooling at 1 T. Black lines are fits to a Curie Weiss law. (b) Susceptibilities of powder and single crystals measured along a, b, and c axes of the β-phase at 7 T.

CONCLUSIONS

We have succeeded in mass production of powder and single crystals of candidate Kitaev magnets honeycomb α- and hyperhoneycomb β-Na_2PrO_3 through performing reactions under inert conditions and identification of mineralizing effect of NaOH and Li_2O for the α- and β-polymorphs, respectively. Single crystals of both polymorphs show fully-ordered structures with no site mixing or structural stacking faults. Revised crystal structures are obtained for both polymorphs from refinement of single crystal X-ray diffraction data. In both structures Pr^{4+} ions realize threefold-coordinated lattices of spin-orbit entangled magnetic moments inside edge sharing octahedra, as required for Kitaev and related models with anisotropic bond-dependent exchanges. The different character of the orbitals mediating the superexchange interactions as well as the different local octahedral distortions could potentially realize distinct regimes of frustrated bond-dependent spin Hamiltonians compared to the much-explored 4d and 5d Kitaev materials.

ACKNOWLEDGEMENTS

This research was supported by the European Research Council under the European Union's Horizon 2020 Research and Innovation Programme Grant Agreement Number 788814 (EQFT). RO acknowledges support from JSPS KAKENHI (Grant No. 23K19027JST) and JST ASPIRE (Grant No. JPMJAP2314).

Table IV. Crystallographic data and the results of structural refinement for α-Na_2PrO_3 from single-crystal X-ray data at 293(2) K. Peaks with $I > 2\sigma(I)$ are defined as observed ones. We use the $C2/c$ space group setting with unique axis b and cell choice 1 (origin at $\bar{1}$ on c-glide plane). Atomic fractional coordinates, and equivalent isotropic U_{iso} and anisotropic U_{ij} displacement parameters (in units of 10^{-3}Å^2) with estimated standard deviations in parentheses.

Formula	α-Na_2PrO_3
Space group	$C2/c$
a (Å)	5.9559(2)
b (Å)	10.3371(3)
c (Å)	11.2069(4)
β (°)	100.423(3)
V (Å^3)	678.59(3)
Z	8
μ (mm^{-1})	14.418
F_{000}	840
$R_{p,obs}$	1.94
$R_{p,all}$	2.31
$R_{wp,obs}$	3.69
$R_{wp,\ all}$	3.87
R_{int}	4.29
Index range	$-8 < h < 7$
	$-14 < k < 13$
	$-15 < l < 15$
$N_{measured}$	8432
N_{unique}	900
N_{obs}	837
N_{param}	59
Crystal size (μm^3)	100×50×10
extinction coefficient ξ	6.9(2) × 10^{-3}

Atom	Wyckoff	x	y	z	U_{iso}	U_{11}	U_{22}	U_{33}	U_{12}	U_{13}	U_{23}
Pr1	4*e*	0	0.58165(2)	1/4	5.21(8)	4.9(1)	4.4(1)	6.2(1)	0	0.7(1)	0
Pr2	4*e*	0	0.24890(2)	1/4	5.36(9)	5.2(1)	4.4(1)	6.4(1)	0	0.8(1)	0
Na1	4*e*	0	0.9155(1)	1/4	7.8(5)	4.2(9)	5.5(9)	14(1)	0	2.1(8)	0
Na2	4*c*	1/4	1/4	0	15.1(4)	18(1)	17(1)	10(1)	0.4(7)	3.8(8)	5.2(8)
Na3	8*f*	0.2635(2)	0.5786(1)	0.0000(1)	13.7(3)	13.0(7)	17.5(8)	9.6(8)	3.0(5)	-0.4(6)	-3.5(5)
O1	8*f*	0.1468(3)	0.7319(2)	0.1432(2)	7.7(5)	9(1)	8.0(1)	6(1)	0.3(8)	-0.5(9)	0.7(9)
O2	8*f*	0.0983(4)	0.4157(2)	0.1428(2)	8.1(5)	8(1)	10(1)	7(1)	-0.2(7)	1.7(9)	0.4(8)
O3	8*f*	0.1442(4)	0.0975(2)	0.1396(2)	8.3(5)	9(1)	10(1)	6(1)	-0.3(7)	1.3(9)	-0.5(8)

Table V. Comparison of the *y* parameter and occupancy of metal atoms in the honeycomb layer used in the various structural models of α-Na_2PrO_3. The notation of each atom is modified from that of refs.[32, 34] to match that of our single crystal study. The space group is *C*2/*c* in all the models and Pr1, Pr2, and Na1 are located at 4*e* (0, *y*, 1/4) site. In powder refinement, consideration of metal atom site-mixing leads to better refinement due to the presence of stacking fault (See the main text for the detail)[32, 34]. The estimated standard deviations of the refined values are shown in parentheses.

		This study		Hinatsu *et al.*[32]
Method		Single crystal	Powder Rietveld refinement	Powder Rietveld refinement
Pr1	*y*	0.58165(2)	0.58165	0.5646(9)
	Occupancy of Pr/Na	1/0	0.774(3)/0.226(3)	0.34(1)/0.66(1)
Pr2	*y*	0.24890(2)	0.2489	0.2494(6)
	Occupancy of Pr/Na	1/0	0.774(3)/0.226(3)	1/0
Na1	*y*	0.9155(1)	0.9155	0.9181(7)
	Occupancy of Na/Pr	1/0	0.547(6)/0.453(4)	0.34(1)/0.66(1)

Table VI. Crystallographic data and the results of structural refinement of β-Na_2PrO_3 from single-crystal X-ray data at 293(2) K (reproduced from Ref.[38]). We use origin choice 2 for the *Fddd* space group (with inversion at origin). Peaks with $I > 2\sigma(I)$ are defined as observed ones. Atomic coordinates, and equivalent isotropic U_{iso} and anisotropic U_{ij} displacement parameters (in units of 10^{-3}Å^2) with the estimated standard deviations in parentheses.

Formula	Na_2PrO_3
Space group	*Fddd*
a (Å)	6.7641(2)
b (Å)	9.7866(4)
c (Å)	20.5517(6)
V (Å^3)	1360.47(8)
Z	16
μ (mm^{-1})	14.383
F_{000}	1680
$R_{p,obs}$	1.85
$R_{p,all}$	3.09
$R_{wp,obs}$	3.25
$R_{wp,all}$	3.72
R_{int}	5.88
Index range	$-9 < h < 9$
	$-13 < k < 12$
	$-27 < l < 26$
$N_{measured}$	4958
N_{unique}	464
N_{obs}	325
N_{param}	31
Crystal size (μm^3)	170×95×31
extinction coefficient ξ	8.0(3) × 10^{-4}

Atom	Wyckoff	x	y	z	U_{iso}	U_{11}	U_{22}	U_{33}	U_{12}	U_{13}	U_{23}
Pr1	16*g*	1/8	1/8	0.70879(1)	6.4(1)	7.9(2)	6.8(2)	4.7(2)	0.7(2)	0	0
Na1	16*g*	1/8	1/8	0.0463(1)	15.6(5)	8(1)	25(1)	13(1)	2(2)	0	0
Na2	16*g*	1/8	1/8	0.8796(1)	11.3(5)	15(1)	10(1)	9(1)	5(1)	0	0
O1	16*e*	0.8400(5)	1/8	1/8	10.0(9)	11(2)	10(2)	9(2)	0	0	0.5(18)
O2	32*h*	0.6384(5)	0.3522(3)	0.0336(1)	9.7(6)	10(2)	11(1)	9(1)	1(2)	0.5(12)	-0.9(11)

Table VII. Bond lengths and bond angles of the nearest Pr-O-Pr triangle for α- and β-Na_2PrO_3 at 293 K with estimated standard deviations in parentheses.

Compound	Pr-O-Pr	d_{Pr-Pr} (Å)	$\theta_{Pr-O-Pr}$ (°)
α-Na_2PrO_3	Pr1-O1-Pr2	3.4434(2)	100.93(6)
	Pr1-O2-Pr2	3.4397(4)	100.6(1)
	Pr1-O3-Pr2	3.4434(2)	99.33(8)
β-Na_2PrO_3	Pr1-O1-Pr1	3.4442(6)	99.6(1)
	Pr1-O2-Pr1	3.4226(3)	100.2(1)

REFERENCES

(1) Balents, L. Spin liquids in frustrated magnets. *Nature* **2010**, *464* (7286), 199-208.
(2) Broholm, C.; Cava, R. J.; Kivelson, S. A.; Nocera, D. G.; Norman, M. R.; Senthil, T. Quantum spin liquids. *Science* **2020**, *367* (6475).
(3) Savary, L.; Balents, L. Quantum spin liquids: a review. *Rep. Prog. Phys.* **2017**, *80* (1), 016502.
(4) Kitaev, A. Anyons in an exactly solved model and beyond. *Ann. Phys. (N. Y.)* **2006**, *321* (1), 2-111.
(5) Motome, Y.; Sano, R.; Jang, S.; Sugita, Y.; Kato, Y. Materials design of Kitaev spin liquids beyond the Jackeli–Khaliullin mechanism. *J. Phys.: Condens. Matter* **2020**, *32* (40), 404001.
(6) Takagi, H.; Takayama, T.; Jackeli, G.; Khaliullin, G.; Nagler, S. E. Concept and realization of Kitaev quantum spin liquids. *Nat. Rev. Phys.* **2019**, *1* (4), 264-280.
(7) Trebst, S.; Hickey, C. Kitaev materials. *Phys. Rep.* **2022**, *950*, 1-37.
(8) Hwan Chun, S.; Kim, J.-W.; Kim, J.; Zheng, H.; Stoumpos, C. C.; Malliakas, C.; Mitchell, J.; Mehlawat, K.; Singh, Y.; Choi, Y. Direct evidence for dominant bond-directional interactions in a honeycomb lattice iridate Na_2IrO_3. *Nat. Phys.* **2015**, *11* (6), 462-466.

(9) Kasahara, Y.; Ohnishi, T.; Mizukami, Y.; Tanaka, O.; Ma, S.; Sugii, K.; Kurita, N.; Tanaka, H.; Nasu, J.; Motome, Y. Majorana quantization and half-integer thermal quantum Hall effect in a Kitaev spin liquid. *Nature* **2018**, *559* (7713), 227-231.
(10) Banerjee, A.; Yan, J.; Knolle, J.; Bridges, C. A.; Stone, M. B.; Lumsden, M. D.; Mandrus, D. G.; Tennant, D. A.; Moessner, R.; Nagler, S. E. Neutron scattering in the proximate quantum spin liquid α-$RuCl_3$. *Science* **2017**, *356* (6342), 1055-1059.
(11) Mandal, S.; Surendran, N. Exactly solvable Kitaev model in three dimensions. *Phy. Rev. B* **2009**, *79* (2), 024426.
(12) Nasu, J.; Udagawa, M.; Motome, Y. Vaporization of Kitaev spin liquids. *Phys. Rev. Lett.* **2014**, *113* (19), 197205.
(13) Takayama, T.; Kato, A.; Dinnebier, R.; Nuss, J.; Kono, H.; Veiga, L.; Fabbris, G.; Haskel, D.; Takagi, H. Hyperhoneycomb Iridate β−Li_2IrO_3 as a Platform for Kitaev Magnetism. *Phys. Rev. Lett.* **2015**, *114* (7), 077202.
(14) Biffin, A.; Johnson, R.; Choi, S.; Freund, F.; Manni, S.; Bombardi, A.; Manuel, P.; Gegenwart, P.; Coldea, R. β−Li_2IrO_3: Full solution via magnetic resonant x-ray diffraction. *Phys. Rev. B* **2014**, *90* (20), 205116.
(15) Biffin, A.; Johnson, R.; Kimchi, I.; Morris, R.; Bombardi, A.; Analytis, J.; Vishwanath, A.; Coldea, R. Noncoplanar and Counterrotating Incommensurate Magnetic Order Stabilized by Kitaev Interactions in γ−Li_2IrO_3. *Phys. Rev. Lett.* **2014**, *113* (19), 197201.
(16) Modic, K. A.; Smidt, T. E.; Kimchi, I.; Breznay, N. P.; Biffin, A.; Choi, S.; Johnson, R. D.; Coldea, R.; Watkins-Curry, P.; McCandless, G. T. Realization of a three-dimensional spin–anisotropic harmonic honeycomb iridate. *Nat. Commun.* **2014**, *5* (1), 4203.
(17) Haraguchi, Y.; Matsuo, A.; Kindo, K.; Katori, H. A. Quantum paramagnetism in the hyperhoneycomb Kitaev magnet β−$ZnIrO_3$. *Phys. Rev. Mater.* **2022**, *6* (2), L021401.
(18) Lea, K.; Leask, M.; Wolf, W. The raising of angular momentum degeneracy of f-electron terms by cubic crystal fields. *J. Phys. Chem. Solids* **1962**, *23* (10), 1381-1405.
(19) Gardner, J. S.; Gingras, M. J.; Greedan, J. E. Magnetic pyrochlore oxides. *Rev. Mod. Phys.* **2010**, *82* (1), 53.
(20) Liu, W.; Zhang, Z.; Ji, J.; Liu, Y.; Li, J.; Wang, X.; Lei, H.; Chen, G.; Zhang, Q. Rare-earth chalcogenides: A large family of triangular lattice spin liquid candidates. *Chin. Phys. Lett.* **2018**, *35* (11), 117501.
(21) Bordelon, M. M.; Kenney, E.; Liu, C.; Hogan, T.; Posthuma, L.; Kavand, M.; Lyu, Y.; Sherwin, M.; Butch, N. P.; Brown, C. Field-tunable quantum disordered ground state in the triangular-lattice antiferromagnet $NaYbO_2$. *Nat. Phys.* **2019**, *15* (10), 1058-1064.
(22) Shen, Y.; Li, Y.-D.; Wo, H.; Li, Y.; Shen, S.; Pan, B.; Wang, Q.; Walker, H.; Steffens, P.; Boehm, M. Evidence for a spinon Fermi surface in a triangular-lattice quantum-spin-liquid candidate. *Nature* **2016**, *540* (7634), 559-562.
(23) Dai, P.-L.; Zhang, G.; Xie, Y.; Duan, C.; Gao, Y.; Zhu, Z.; Feng, E.; Tao, Z.; Huang, C.-L.; Cao, H. Spinon fermi surface spin liquid in a triangular lattice antiferromagnet $NaYbSe_2$. *Phys. Rev. X* **2021**, *11* (2), 021044.
(24) Xing, J.; Feng, E.; Liu, Y.; Emmanouilidou, E.; Hu, C.; Liu, J.; Graf, D.; Ramirez, A. P.; Chen, G.; Cao, H. Néel-type antiferromagnetic order and magnetic field–temperature phase diagram in the spin-1/2 rare-earth honeycomb compound $YbCl_3$. *Phys. Rev. B* **2020**, *102* (1), 014427.
(25) Matsumoto, Y.; Schnierer, S.; Bruin, J. A.; Nuss, J.; Reiss, P.; Jackeli, G.; Kitagawa, K.; Takagi, H. A quantum critical Bose gas of magnons in the quasi-two-dimensional antiferromagnet $YbCl_3$ under magnetic fields. *Nat. Phys.* **2024**, 1-8.
(26) Ishikawa, H.; Kurihara, R.; Yajima, T.; Nishio-Hamane, D.; Shimizu, Y.; Sakakibara, T.; Matsuo, A.; Kindo, K. SmI_3: $4f^5$ honeycomb magnet with spin-orbital entangled Γ_7 Kramers doublet. *Phys. Rev. Mater.* **2022**, *6* (6), 064405.
(27) Jang, S.-H.; Motome, Y. Exploring rare-earth Kitaev magnets by massive-scale computational analysis. *arXiv preprint arXiv:2402.18837* **2024**.
(28) Jang, S.-H.; Sano, R.; Kato, Y.; Motome, Y. Computational design of *f*-electron Kitaev magnets: Honeycomb and hyperhoneycomb compounds A_2PrO_3 (A= alkali metals). *Phys. Rev. Mater.* **2020**, *4* (10), 104420.
(29) Jang, S.-H.; Sano, R.; Kato, Y.; Motome, Y. Antiferromagnetic Kitaev interaction in f-electron based honeycomb magnets. *Phys. Rev. B* **2019**, *99* (24), 241106.
(30) Jang, S.-H.; Motome, Y. Exchange Interactions in Rare-earth Magnets A_2PrO_3 (*A* = alkali metals): Revisited. *arXiv preprint arXiv:2404.17058* **2024**.
(31) Shannon, R. T.; Prewitt, C. T. Effective ionic radii in oxides and fluorides. *Acta. Crystallogr. B* **1969**, *25* (5), 925-946.
(32) Hinatsu, Y.; Doi, Y. Crystal structures and magnetic properties of alkali-metal lanthanide oxides A_2LnO_3 (A = Li, Na; Ln= Ce, Pr, Tb). *J. Alloys Compd.* **2006**, *418* (1-2), 155-160.
(33) Daum, M. J.; Ramanathan, A.; Kolesnikov, A. I.; Calder, S.; Mourigal, M.; La Pierre, H. S. Collective excitations in the tetravalent lanthanide honeycomb antiferromagnet Na_2PrO_3. *Phys. Rev. B* **2021**, *103* (12), L121109.
(34) Ramanathan, A.; Leisen, J. E.; La Pierre, H. S. In-plane cation ordering and sodium displacements in layered honeycomb oxides with tetravalent lanthanides: Na_2LnO_3 (Ln = Ce, Pr, and Tb). *Inorg. Chem.* **2021**, *60* (3), 1398-1410.
(35) Wolf, R.; Hoppe, R. On Na_2PrO_3 and Na_2TbO_3. *Z. Anorg. Allg. Chem.* **1988**, *556 (1),* 97-108.
(36) O'Malley, M. J.; Verweij, H.; Woodward, P. M. Structure and properties of ordered Li_2IrO_3 and Li_2PtO_3. *J. Solid State Chem.* **2008**, *181* (8), 1803-1809.
(37) Zintl, E.; Morawietz, W. Doppeloxyde mit Steinsalzstruktur. *Z. Anorg. Allg. Chem.* **1940**, *245* (1), 26-31.
(38) Okuma, R.; MacFarquharson, K.; Johnson, R. D.; Voneshen, D.; Manuel, P.; Coldea, R. Compass-model physics on the hyperhoneycomb lattice in the extreme spin-orbit regime. *submitted*.
(39) Rodríguez-Carvajal, J. Recent advances in magnetic structure determination by neutron powder diffraction. *Phys. B: Condens. Matter* **1993**, *192* (1-2), 55-69.
(40) Burla, M. C.; Caliandro, R.; Carrozzini, B.; Cascarano, G. L.; Cuocci, C.; Giacovazzo, C.; Mallamo, M.; Mazzone, A.; Polidori, G. Crystal structure determination and refinement via SIR2014. *J. Appl. Crystallogr.* **2015**, *48* (1), 306-309.
(41) Dolomanov, O. V.; Bourhis, L. J.; Gildea, R. J.; Howard, J. A.; Puschmann, H. OLEX2: a complete structure solution, refinement and analysis program. *J. Appl. Crystallogr.* **2009**, *42* (2), 339-341.
(42) Momma, K.; Izumi, F. VESTA 3 for three-dimensional visualization of crystal, volumetric and morphology data. *J. Appl. Crystallogr.* **2011**, *44* (6), 1272-1276.
(43) Choi, S.; Coldea, R.; Kolmogorov, A.; Lancaster, T.; Mazin, I.; Blundell, S.; Radaelli, P.; Singh, Y.; Gegenwart, P.; Choi, K. Spin waves and revised crystal structure of honeycomb iridate Na_2IrO_3. *Phys. Rev. Lett.* **2012**, *108* (12), 127204.
(44) Williams, S.; Johnson, R.; Freund, F.; Choi, S.; Jesche, A.; Kimchi, I.; Manni, S.; Bombardi, A.; Manuel, P.; Gegenwart, P. Incommensurate counterrotating magnetic order stabilized by Kitaev interactions in the layered honeycomb α−Li_2IrO_3. *Phys. Rev. B* **2016**, *93* (19), 195158.
(45) Johnson, R. D.; Williams, S.; Haghighirad, A.; Singleton, J.; Zapf, V.; Manuel, P.; Mazin, I.; Li, Y.; Jeschke, H. O.; Valentí, R. Monoclinic crystal structure of α−$RuCl_3$ and the zigzag antiferromagnetic ground state. *Phys. Rev. B* **2015**, *92* (23), 235119.
(46) Harris, E.; Mellor, J.; Parke, S. Electron paramagnetic resonance of tetravalent praseodymium in zircon. *Phys. Status Solidi B* **1984**, *122* (2), 757-760.

(47) Ramanathan, A.; Kaplan, J.; Sergentu, D.-C.; Branson, J. A.; Ozerov, M.; Kolesnikov, A. I.; Minasian, S. G.; Autschbach, J.; Freeland, J. W.; Jiang, Z. Chemical design of electronic and magnetic energy scales of tetravalent praseodymium materials. *Nat. Commun.* **2023**, *14* (1), 3134.
(48) Gompa, T. P.; Ramanathan, A.; Rice, N. T.; La Pierre, H. S. The chemical and physical properties of tetravalent lanthanides: Pr, Nd, Tb, and Dy. *Dalton Trans.* **2020**, *49* (45), 15945-15987.